

A physics-informed transformer neural operator for learning generalized solutions of initial boundary value problems

Sumanth Kumar Boya ·
Deepak Subramani

Received: date / Accepted: date

Abstract Initial boundary value problems arise commonly in applications with engineering and natural systems governed by nonlinear partial differential equations (PDEs). Operator learning is an emerging field for solving these equations by using a neural network to learn a map between infinite dimensional input and output function spaces. These neural operators are trained using a combination of data (observations or simulations) and PDE-residuals (physics-loss). A major drawback of existing neural approaches is the requirement to retrain with new initial/boundary conditions, and the necessity for a large amount of simulation data for training. We develop a physics-informed transformer neural operator (named PINTO) that efficiently generalizes to unseen initial and boundary conditions, trained in a simulation-free setting using only physics loss. The main innovation lies in our new iterative kernel integral operator units, implemented using cross-attention, to transform the PDE solution's domain points into an initial/boundary condition-aware representation vector, enabling efficient learning of the solution function for new scenarios. The PINTO architecture is applied to simulate the solutions of important equations used in engineering applications: advection, Burgers, and steady and unsteady Navier-Stokes equations (three flow scenarios). For these five test cases, we show that the relative errors during testing under challenging conditions of unseen initial/boundary conditions are only one-fifth to one-third of other leading physics informed operator learning methods. Moreover, our PINTO model is able to accurately solve the advection and Burgers equations at time steps that are not included in the training collocation points. The code is available at <https://github.com/quest-lab-iisc/PINTO>.

Corresponding Author: Deepak Subramani

Department of Computational and Data Sciences,
Indian Institute of Science, Bangalore 560012 India
Tel.: +91-080-2293 2058
E-mail: deepakns@iisc.ac.in

Keywords Nonlinear mapping · Operator learning · Transformer operator · Scientific machine learning · Physics-informed deep learning · Initial and boundary generalization · AI for PDEs

1 Introduction

Solving initial boundary value problems (IBVPs) with governing partial differential equations (PDEs) is essential to understand and characterize the dynamics of natural and engineering systems. Traditionally, numerical methods (e.g., finite difference, finite element, finite volume, or spectral) are employed to solve PDEs. In recent decades, scientists have created high-performance computing software designed to solve IBVP and parametric PDE, enabling their use as forward models in engineering design (Wang et al., 2022a; Ion et al., 2022; Richter et al., 2021; Heermann and Burkitt, 2012). However, for a new set of initial and/or boundary conditions, the numerical method must be applied afresh to solve the PDE as a new problem by spending significant compute resources. In contrast, contemporary artificial intelligence tasks in computer vision and natural language processing involve running a trained model (inference), which is computationally less expensive, for new scenarios. Those fields have benefitted from neural models that generalize to new situations well. The promise and application scope of such PDE solving models that could be trained once and used for fast simulation in new situations is appealing. Thus, over the past several years, the development of neural models for simulating systems governed by PDEs has picked up pace. Our goal is to develop a neural model for learning generalized solutions of IBVPs.

Deep neural networks that solve PDEs are broadly classified into two categories: *(i)* neural operators that learn the mapping between function spaces (input function of say parameters and output function of the solution) such as DeepONets, Fourier neural operators (FNO), physics-informed neural operators (PINO), and graph neural operators (GNO) (Li et al., 2020b,a; Lu et al., 2021a; You et al., 2022a; Kovachki et al., 2023a) and *(ii)* neural networks that learn a map between the PDE’s space-time domain and the solution function (Raissi et al., 2019; Lu et al., 2021b; Karniadakis et al., 2021; Yang et al., 2021; Cai et al., 2021). Both approaches can be trained using a combination of simulation data and PDE-residuals. When training is dominated by PDE-residuals (also called *physics loss*), the approach is called unsupervised, and a qualifier of *physics-informed* is added (e.g., Physics-Informed Neural Operator: PINO; Physics-Informed Neural Network: PINN). The physics loss is calculated using automatic differentiation to compute the partial derivatives of the solution with respect to the coordinates of the space-time domain. However, it must be noted that supervised training with simulation data obtained from a classical numerical method is also sometimes called physics-informed.

A PINN model only learns the map for one instance of the PDE and requires re-training for solving with new initial/boundary conditions, much like traditional numerical solvers. On the other hand, neural operators can learn

a map between an initial/boundary function and a solution function, thereby achieving generalization to unseen conditions for a particular PDE. However, the current leading neural operators such as the Fourier neural operator (FNO) (Li et al., 2020a; Pathak et al., 2022; Wen et al., 2022; Bonev et al., 2023; You et al., 2022b; Li et al., 2023b; George et al., 2024; Kovachki et al., 2021a, 2023b; Lehmann et al., 2024), DeepONet (Wang et al., 2021; Lu et al., 2021a; Lanthaler et al., 2022; He et al., 2024; Xu et al., 2023; Li et al., 2023a; Goswami et al., 2022, 2023, 2024; Haghghat et al., 2024), Graph neural operator (Li et al., 2020b,c), Convolutional neural operators (Raonic et al., 2024), Complex neural operator (Tiwari et al., 2023), Wavelet neural operator (Gupta et al., 2021; Tripura and Chakraborty, 2023; Rani et al., 2023), Laplacian neural operator (Pang et al., 2020; Cao et al., 2024), RiemannONets (Peyvan et al., 2024), Geometry informed neural operator (GINO) (Li et al., 2024b), Diffeomorphism Neural Operator (Zhao et al., 2024), Spectral neural operator (Fanaskov and Oseledets, 2023; Rafiq et al., 2022), operator transformer (Hao et al., 2023; Li et al., 2022; Shih et al., 2025), Local neural operator (Li et al., 2024a), and Peridynamic neural operators (Jafarzadeh et al., 2024) are all trained using a vast amount of simulation data. The physics-informed variant of these methods also needs some amount of simulation data (perhaps in a coarse domain) for training. Moreover, as we show in this paper, the current leading architectures that can be trained without any simulation data are not efficient in practice for initial/boundary condition generalization.

For learning generalized solutions of IBVPs, we develop the Physics-Informed Neural Transformer Operator (PINTO) that learns a map between the initial/boundary function space and the PDE’s solution function space. The primary novelty is introducing a cross-attention unit that modulates the internal representation of the domain’s space-time coordinates with information from the initial/boundary function, so that a generalized solution is obtained for any unseen initial/boundary function. Our model is trained with physics loss, without using simulation data.

The applications that can benefit from the developed architecture are vast. For example, it could be used as surrogate models for faster inference (Chennault et al., 2021; Arcucci et al., 2020) and as solvers (Wu et al., 2021; Fablet et al., 2021) in data assimilation and inverse problems. It can replace traditional CFD solvers in applications that require fluid flow simulations such as autonomous path planning (Chowdhury et al., 2023), biomedical fluid dynamics (Kelley and Thomas, 2023), mask design (Mittal et al., 2023), and wake modeling in wind farms (Breton et al., 2017).

1.1 Related work:

Neural operators to learn maps between infinite-dimensional input and output spaces have gained tremendous popularity in recent years. Concurrent work on branch-trunk network DeepONet architecture, discretization-dependent convolutional neural operators, and discretization-invariant Fourier neural oper-

ators has led the way. In the DeepONet architecture, a trunk net encodes the coordinates of the space-time domain of the PDE, and a branch net encodes the discrete input function space (Lu et al., 2021a). The representations are merged using a Hadamard product. This operator was trained using simulation data. Later work extended the setup to situations where data availability is sparse by introducing PDE-residual loss as a physics-informed regularizer during DeepONet training (Wang et al., 2021, 2022b; Goswami et al., 2023). Extensions have been reported to multiple input functions (Jin et al., 2022), efficient numerics (Mandl et al., 2024), and training using the variational form of PDE residuals (Goswami et al., 2022).

The Fourier neural operator (FNO) is a discretization invariant neural operator that is emerging as a potential universal approximator (Li et al., 2020a; Kovachki et al., 2021a, 2023a). Using convolutions within the spectral domain facilitated by the Fast Fourier Transform, FNOs learn the mapping between function spaces. However, they require a substantial amount of simulation data for training purposes. Enhancements in FNOs have been made by incorporating PDE-residual loss in their training, although they still require simulation data, but with reduced resolution (Li et al., 2024c). Deep implicit FNO has been used to learn the mapping between loading conditions and the response of heterogeneous materials without predefined constitutive models or microstructure measurements (You et al., 2022b). An FNO-based architecture has been developed to simulate a highly complex multiphase CO₂ water problem with wide ranges of porosity heterogeneity, anisotropy, reservoir conditions, injection configurations, flow rates, and multiphase flow properties using large simulation datasets (Wen et al., 2022). Fourier neural operator has been used for full wave inversion to infer subsurface structure information from seismic waveform data (Zhu et al., 2023).

Transformers have been suggested as neural operators because they are inherently capable of mapping functional spaces over irregular and nonuniform grids. Data-driven operator learning has been conducted using an attention mechanism reminiscent of Galerkin methods (Cao, 2021). With this Galerkin-like attention, an encoder-decoder transformer model was developed to handle both uniform and varied discretization grids (Li et al., 2022). To solve complex PDEs involving multiple input functions and irregular grids, a general neural operator transformer Hao et al. (2023) was introduced. The authors implemented a heterogeneous normalized attention mechanism to decrease the computational cost of calculating attention scores and introduced a geometric gating mechanism to address multiscale problems.

Recently, an approach was proposed to solve PDEs for multiple initial and boundary conditions without retraining the model using modifications to the gradient descent algorithm (Navaneeth et al., 2024). They encode the prior knowledge of the governing equations through a stochastic projection-based gradient (Navaneeth and Chakraborty, 2023) that is computationally efficient in evaluating gradients for high-dimensional problems. Still, it comes with the cost of approximation and randomness in evaluating gradients. Their

architecture learns the map between the initial conditions and the solution space.

Though DeepONet achieved a wide range of applicability in approximating nonlinear operators, it has issues with scalability for high-dimensional PDEs due to data requirements. Also, the discrete input function requires data on a pre-defined grid that makes generalization difficult. FNOs and other recent neural operators mentioned in the introduction cannot be trained reliably without simulation data, restricting their applications to users without access to simulation data. The attention mechanism is a promising route for developing neural operators, and we utilize the same in our work. As a reference, we used the solution obtained by a physics-informed DeepONet (PI-DeepONet) to benchmark the performance of our proposed model.

1.2 Key contributions

Our main contributions are: *(i)* development of a new cross-attention mechanism, grounded in neural operator theory, for an efficient neural operator that generalizes the solution of initial boundary value problems for unseen initial/boundary conditions; *(ii)* training of the neural operator is using only physics loss, without data from numerical simulations; *(iii)* better simulation of solution for challenging benchmark test cases including the advection equation, Burger’s equation, Navier Stokes Equations in three different test cases; and *(iv)* ability to simulate solutions outside the temporal domain used for training. The success of our new neural operator is attributable to the transformation of the PDE solution’s domain query point (spatio-temporal coordinates) into a boundary-aware vector through multiple cross-attention units (iterative kernel integral operator).

In the remaining sections, we first describe the mathematical problem statement, neural operator theory, and practical implementation of our new architecture (Sect. 2). Next, we apply the new network for the 1D Advection, 1D nonlinear Burgers, the Kovasznay flow, the Beltrami flow, and the lid-driven cavity flow test cases (Sect. 3). We compare our results with other leading physics-informed neural operator architectures that can be trained without simulation data (i.e., PI-DeepONet) and showcase the advantages of the new model for initial and boundary condition generalization. In Sect. 4, we discuss the computational complexity, difference of PINTO from other physics-informed neural networks and neural operators, how to leverage our new cross-attention unit in other operators and limitations of PINN models. Finally, we conclude with a summary and directions for future work (Sect. 5).

2 Development of Physics-Informed Transformer Neural Operator

2.1 Neural Operator Definition and Loss Function

Consider a general partial differential equation (PDE) of the form

$$\mathcal{N}(h, X; \alpha) = f \text{ in } \Omega, \quad (1a)$$

$$\mathcal{B}(h, X_b) = b \text{ on } \partial\Omega, \quad (1b)$$

where $h \in \mathcal{H} \subseteq \mathbb{R}^s$ is the s -dimensional solution field from the solution space $\mathcal{H} \subset L^2(\Omega, \mathcal{R}^s)$, \mathcal{N} is a general nonlinear differential operator with spatial and temporal partial derivatives, $X \in \Omega \subseteq \mathbb{R}^d$ is a d -dimensional coordinate from the spatiotemporal domain Ω , α is the PDE's parameter vector, f is a forcing term, \mathcal{B} is the initial/boundary operator, $X_b \in \partial\Omega \subseteq \mathcal{R}^d$ is the d -dimensional initial/boundary coordinate from the domain's boundary $\partial\Omega$ and b is the imposed initial/boundary condition vector.

The initial boundary value problem can be expressed as follows. Let $\mathcal{A} \subset L^2(\partial\Omega, \mathcal{R}^d)$ be the functional space of the initial/boundary condition. For an imposed initial/boundary condition $b \in \mathcal{A}$, there is a solution $h \in \mathcal{H}$ that satisfies the PDE (1). Thus, there exists a map $\mathcal{G} : \mathcal{A} \rightarrow \mathcal{H}$ that for every observed pair (b, h) satisfies $h = \mathcal{G}(b)$. The solution field is accessible at any $X \in \Omega$ as $h(X) = \mathcal{G}(b)(X)$. We develop a parametrized neural operator $\mathcal{G}_\theta(X, b; \Theta^*)$, $\Theta^* \in \mathcal{R}^p$ that approximates \mathcal{G} and generalizes to predict the correct $h(X)$ for any $b \in \mathcal{A}$. Here, p is the dimension of the parameter vector of the neural network.

We propose the use of PDE-residuals (physics-loss) to train \mathcal{G}_θ . The set of equations that \mathcal{G}_θ must satisfy is as follows.

$$\mathcal{N}(\mathcal{G}_\theta(X, b; \Theta^*), X; \alpha) = f \text{ on } \Omega, \quad (2a)$$

$$\mathcal{B}(\mathcal{G}_\theta(X, b; \Theta^*), X_b) = b \text{ on } \partial\Omega \forall b \in \mathcal{B}. \quad (2b)$$

Thus, the training objective to compute the optimal Θ^* by empirical risk minimization can be expressed as

$$\min_{\Theta} \sum_{k=1}^K \left\{ \frac{\lambda_1}{N_c} \sum_{j=1}^{N_c} |f_{c,k}^j - \mathcal{N}(\mathcal{G}_\theta(\Theta; X_{c,k}^j); \alpha)|^2 + \frac{\lambda_2}{N_{ib}} \sum_{j=1}^{N_{ib}} |b_{ib,k}^j - \mathcal{B}(\mathcal{G}_\theta(\Theta; X_{ib,k}^j))|^2 \right\}, \quad (3)$$

where $k = [1, 2, \dots, K]$ is the set of discrete boundary conditions sampled from \mathcal{A} such that $b_k \in \mathcal{A}$, λ_1, λ_2 are the weights to balance the different terms in the loss function. The first term in the above equation (3) is the physics loss and the second term forces the neural operator to satisfy the provided boundary conditions. Now the goal is to develop an architecture for \mathcal{G}_θ that is efficient in learning the representation of the PDE's solution for any initial and boundary condition. In what follows, we develop a neural transformer architecture for the same.

2.2 Cross Attention Neural Operator Theory

We build the parametric map $\mathcal{G}_\theta: \mathcal{A} \rightarrow \mathcal{H}$ as a composition of neural layers that perform lifting, iterative kernel integration, and projection as follows Li et al. (2023b).

$$\mathcal{G}_\theta := \mathcal{Q} \circ \sigma(\mathcal{W}_T + \mathcal{K}_T + b_T) \circ \cdots \circ \sigma(\mathcal{W}_1 + \mathcal{K}_1 + b_1) \circ \mathcal{P}, \quad (4)$$

where \mathcal{P} is the lifting operator, \mathcal{Q} is the projection operator and the other terms are the $t = 1, \dots, T$ hidden layers that perform iterative kernel integration. Here, σ is the pointwise nonlinear activation function, \mathcal{W}_t is a local linear operator, \mathcal{K}_t is the nonlinear kernel integral operator and b_t is the bias function. These layers map each hidden representation to the next, i.e., $\{v_t: D_t \rightarrow \mathbb{R}^{d_{v_t}}\} \mapsto \{v_{t+1}: D_{t+1} \rightarrow \mathbb{R}^{d_{v_{t+1}}}\}$ using

$$v_{t+1}(x) = \sigma_{t+1} \left(W_t v_t(x) + \int_{D_t} \left(\kappa^{(t)}(x, y) v_t(y) \right) dv_t(y) + b_t(x) \right) \quad \forall x \in D_{t+1}. \quad (5)$$

We propose an encoding layer $\mathcal{P} = W_{qpe}X$ for the lifting operator and a multi-layer perceptron $\mathcal{Q} = MLP(v_T(X))$ for the projection operator. For \mathcal{K}_t , we propose a cross-attention kernel integral operator

$$\mathcal{K}_t = \int_{\partial\Omega} \frac{\exp\left(\frac{\langle A_h v_t(X), B_h W_{bpe} X_b \rangle}{\sqrt{m}}\right)}{\int_{\partial\Omega} \exp\left(\frac{\langle A_h v_t(X), B_h W_{bpe} X_b \rangle}{\sqrt{m}}\right) dX_b} R_h W_{bve} b dX_b, \quad (6)$$

where $v_t(X)$ is the hidden representation of the boundary domain's query point coordinate, W_{bpe} is the encoding matrix for initial/boundary domain's coordinate X_b , W_{bve} is the encoding matrix for the boundary condition function value b , A_h is the linear transformation for the encoded query point, B_h is the linear transformation for the encoded boundary point and R_h is the linear transformation for the encoded boundary function value, m is the dimension of the encoded vectors (hyperparameter) and $\langle \cdot, \cdot \rangle$ is the Euclidean inner product on \mathbb{R}^m .

2.3 Practical Implementation

Fig. 1 illustrates our new Physics-Informed Transformer Neural Operator, named PINTO, that implements the cross-attention integral kernel integral operator. There are three stages of operation. In the first stage, we discretize the boundary function $\mathcal{B}(X_b^i)$ at L discrete points X_b^i , $i = 1, \dots, L$, and encode them using Boundary Value Encoding (BVE) and Boundary Position Encoding (BPE) units. We also encode the solution domain's query point coordinate using Query Point Encoding (QPE) unit. All these encoding units are lifting operators as they encode scalar values as vectors of dimension m . We use dense layers in these units, but note that any other type of layer such as convolution or recurrent could also be used in the approach.

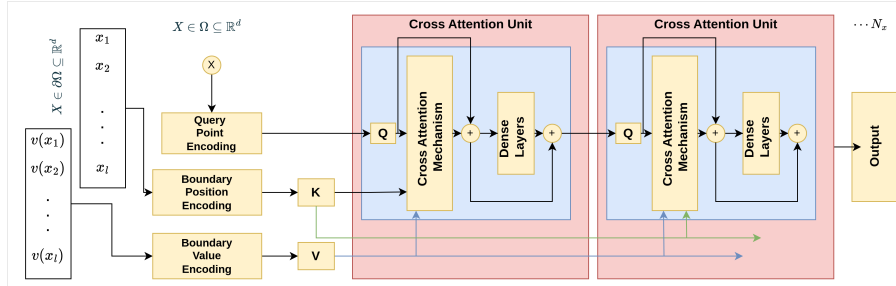


Fig. 1 Schematic of PINTO: Our neural operator has three stages (i) Query Point, Initial/Boundary Point and Initial/Boundary Value (lifting operators) (ii) Cross Attention Units (iterative kernel integral operators) and (iii) output projection dense layers.

In the second stage, the network obtains a boundary-aware query point encoding vector through multiple passes of our new cross-attention units. In each cross-attention unit, the boundary key and value are shared so that the initial/boundary conditions influence the context-aware hidden representation of query points correctly. The vector representation from the QPE is used as the query of the first cross-attention block, and the output of the previous cross-attention unit is used for all subsequent cross-attention units. We implement a deep multihead cross attention unit to increase the generalization ability and learning capacity of the neural operator model. The discrete multihead cross-attention unit is implemented as follows. First, the attention score ζ_i between the encoded query point at the layer t and every i th discrete initial/boundary point and value is calculated as

$$\zeta_i = \left(\sum_{l=1}^L \exp \left(\frac{\langle A_h v_t(X), B_h W_{bpe}(X_b^l) \rangle}{\sqrt{m}} \right) \right)^{-1} \exp \left(\frac{\langle A_h v_t(X), B_h W_{bpe}(X_b^i) \rangle}{\sqrt{m}} \right). \quad (7)$$

Next, the output from the cross-attention unit with H attention heads is calculated with a residual connection and a Swish nonlinear activation function as

$$v_{t+1}(X) = \sigma \left(A_h v_t(X) + \left(\sum_{h=1}^H \sum_{i=1}^L \zeta_i \cdot R_h W_{bve}(B(X_b^i)) \right) \right). \quad (8)$$

In the third and final stage, the encoded query point representation is projected onto the solution space using dense layers.

During training, the data must be prepared such that the QPE unit is exposed to collocation points within the domain where the PDE loss is applied, as well as boundary points where both the boundary condition and the PDE loss are enforced. For each input to the QPE unit, the corresponding boundary conditions and the sequence of their values must be provided to the BPE and BVE units. In the case of Dirichlet boundary conditions, the boundary value is provided directly. However, for Neumann boundary conditions, the derivative values need to be fed to the BVE unit, and the loss function needs to be

modified to account for these conditions. The code, PINTO architecture, and their trained weights have been released on GitHub with a Zenodo DOI Kumar (2024).

3 Applications of PINTO

The performance of PINTO in simulating the solution of IBVPs for unseen initial and boundary conditions is demonstrated by employing the following test cases: (i) 1D-Advection equation, (ii) 1D non-linear Burgers equation, (iii) 2D unsteady Beltrami flow, (iv) 2D steady Kovasznay flow, and (v) 2D steady Lid-driven flow in the $x - y/z$ plane. The first two test cases demonstrate the applicability of our PINTO model in solving initial value problems and providing solutions for unseen times in the temporal domain. The latter ability is absent for the other leading physics-informed neural operators as we show. Numerical solutions of the advection equation from the PDEBENCH dataset (Takamoto et al., 2022), and those of the Burgers equation from an off-the-shelf solver Kovachki et al. (2021b) are used to validate the PINTO simulations. The next three test cases are governed by the Navier-Stokes equations. The third and fourth test cases, namely the Kovasznay and Beltrami flows, have analytical solutions (Kovasznay, 1948; Taylor, 1923) for different Reynolds numbers (Re), which are used to validate the PINTO solutions. These test cases demonstrate the applicability of our PINTO model to solve equations where the initial and boundary conditions vary spatially and temporally. In the fifth test case, called lid-driven cavity flow, we investigate the steady state flow within a vertical cavity where the top lid moves to the right at a constant speed. This flow is a simplified version of the wind-driven ocean flow and finds various practical applications in ocean and atmospheric studies. To validate our PINTO predictions, we obtain numerical solutions of the flow from a Finite Volume code (Ueckermann and Lermusiaux, 2012), where the boundary condition varied is the speed of the lid movement. Note that in all these situations, the validation data is not used for training. Training is performed using only Physics loss and initial/boundary conditions.

The performance of the PINTO model for all numerical examples is compared to the physics-informed DeepONet model (PI-DeepONet) (Lu et al., 2021a; Goswami et al., 2023). Although PI-DeepONet has not been used for learning generalized solutions of IBVPs, we repurposed them to find PDE solutions with different initial/boundary conditions by using the input functions for the branch net as the initial and boundary conditions. PI-DeepONet is chosen as the benchmark for comparison as it can be trained using only physics-loss unlike other neural operators that need some amount of simulation data. Table 1 summarizes the relative error for all test cases. In the upcoming sections, we take a deep dive into each test case. The code and data are available on Zenodo Kumar (2024) and Github.

Table 1 Performance Metrics: Mean relative error (with standard deviation) of the trained PINTO models’ solution when compared with the ground truth (numerical or analytical solution) for seen and unseen initial/boundary conditions. The metrics for PI-DeepONet is shown for comparison.

Test Case	PINTO		PI-DeepONet	
	Seen Conditions	Unseen Conditions	Seen Conditions	Unseen Conditions
1D Advection equation	2.11% (4.01%)	2.85% (4.73%)	1.35% (3.75%)	11.26% (11.42%)
1D Burgers equation	4.81% (4.43%)	5.24% (4.51%)	12.81% (11.85%)	15.03% (10.78%)
Kovaszny Flow	0.037% (0.0325%)	0.41% (2.55%)	0.08% (0.066%)	2.26% (6.54%)
Beltrami Flow	0.53% (0.1%)	0.6% (0.92%)	2.62% (4.19%)	4.89% (12.14%)
Lid Driven Cavity Flow	1.36% (1.44%)	2.78% (2.49%)	1.96% (2.31%)	6.08% (6.61%)

3.1 Advection Equation

As the first test case, we use PINTO to solve the one-dimensional advection equation. The advection equation is a hyperbolic equation used widely for simulating the movement of a conserved scalar in a flow field,

$$\frac{\partial u}{\partial t} + \beta \frac{\partial u}{\partial x} = 0, \text{ in } \Omega = \{(x, t) : x \in [0, 1], t \in (0, \infty)\} \quad (9a)$$

$$u(0, x) = \sum_{k_i=k_1, \dots, k_N} (A_i \sin k_i x + \phi_i), \text{ in } \partial\Omega \quad (9b)$$

where x is the spatial coordinate, t is the temporal coordinate, and β is the constant advection speed. Different initial conditions are generated using the superposition of the sinusoidal wave equation (Eq. 9b), where $k_i = 2\pi\{n_i\}/L_x, i = 1, \dots, N$ whose wave numbers $\{n_i\}$ are random integers in $[1, n_{max}]$, N is an integer that determines how many waves to add, L_x is the domain size, A_i is the amplitude randomly chosen in $[0, 1]$, and ϕ_i is the phase randomly chosen in $(0, 2\pi)$. We set $\beta = 0.1$ for all experiments. We selected 100 initial conditions. For 80 of these initial conditions, the PINTO model is trained using the physics loss Eq. 3. The remaining 20 initial conditions are the unseen situations for which we will evaluate the initial condition generalization ability of PINTO. For validation, we use the PDEBENCH dataset that contains the numerical solutions of the advection equation for these initial conditions solved using a finite difference scheme with 2nd order upwind for time marching and a spatial grid size of 1024 Takamoto et al. (2022). Note that the PINTO model is not trained using the PDEBENCH dataset.

For training PINTO, 2000 collocation, and 250 initial and boundary points are considered in the domain $[0, 1] \times [0, 1]$. For comparison, the PI-DeepONet model is also trained under the same conditions. PINTO predictions, numerical solutions, and relative error across the domain for the two seen and unseen initial conditions are shown in Figure 2. We see that the relative error is low for both seen and unseen initial conditions. PINTO is also able to forecast the solution for times $t > 1$ not included in the training time steps. Figure 3 shows the solution wave at $t = 0.01, 1.0, 2.0$ for two seen and unseen initial conditions, superimposed with the numerical solution from PDEBENCH

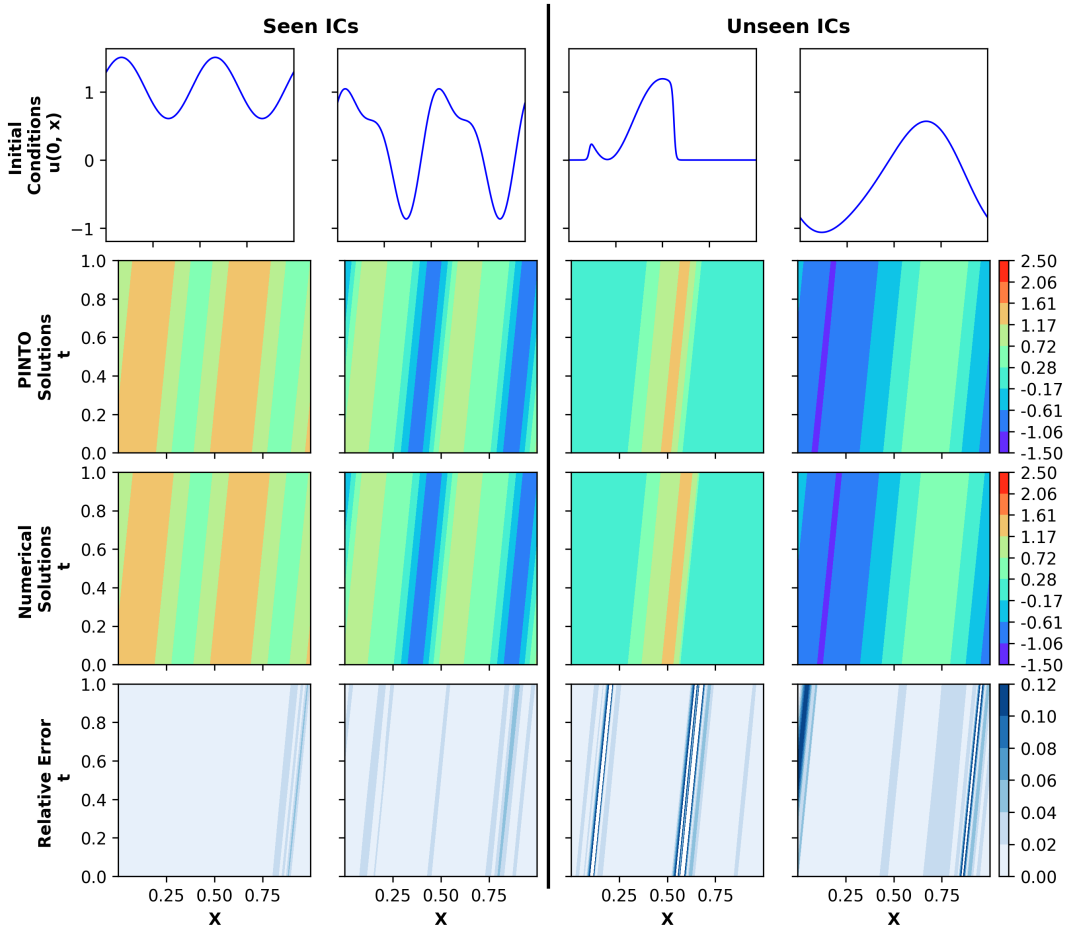


Fig. 2 Advection Equation: Initial conditions (first row), PINTO solutions (second row), corresponding PDEBENCH data (third row) and relative error of PINTO solution (fourth row) for seen (first two columns) and unseen (last two columns) initial conditions.

and the solution from PI-DeepONet. For seen initial conditions, both models generalized well for unseen future time ($t > 1$), whereas for unseen initial conditions, only PINTO predictions are accurate for $t > 1$. The relative errors for all test cases (categorized into seen and unseen initial conditions) of the PINTO solutions and the PI-DeepONet solutions for the advection equation are tabulated in Table 1. The PINTO solution has a smaller relative error of 2.85% compared to the PI-DeepONets 11.26%.

Hyperparameter tuning was performed to select the number of CAUs, sequence length, learning rate, and activation functions using validation on unseen initial conditions, as described in Table 2. Figure 4 shows the learning curves of the PINTO model for various learning rates and sequence lengths.

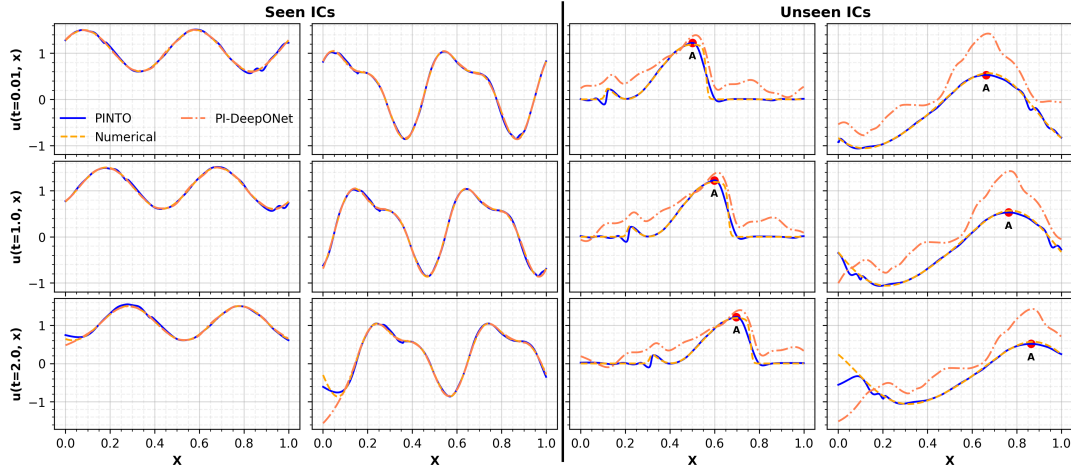


Fig. 3 Advection Equation: PINTO, PI-DeepONet and numerical solutions (PDEBENCH) for seen and unseen initial conditions at $t=0.01, 0.5, 2$. The first two columns are results for seen and the last columns are for the unseen initial conditions. A landmark A is shown in the solution for unseen initial conditions (ICs) to visualize how the wave is propagating in time.

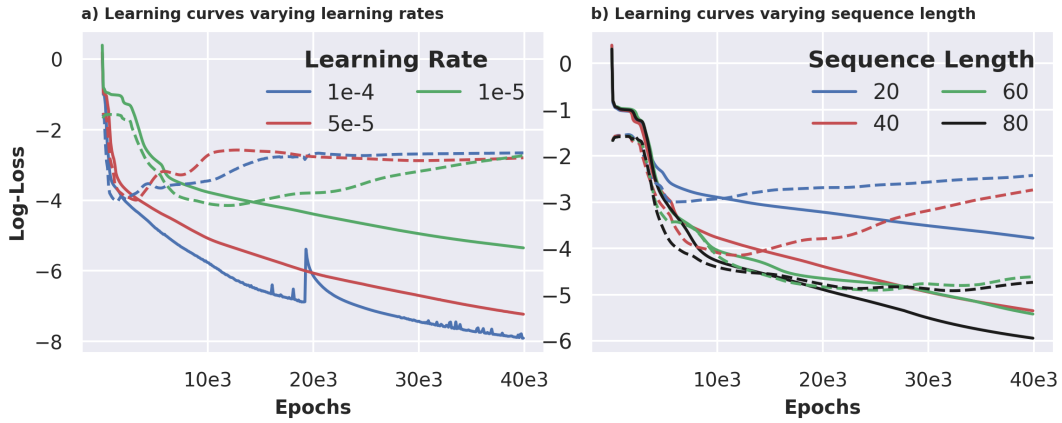


Fig. 4 Learning curves during PINTO training for advection equation: a) Training (solid line) and validation (dashed line) loss curves for different learning rates. b) Training (solid line) and validation (dashed line) loss curves for different sequence lengths of initial conditions for a learning rate of $1e-5$.

Figure 4 shows that lower learning rates and longer sequence lengths result in reduced validation loss. Consequently, the PINTO model was trained for 20000 epochs using the Adam optimizer with a learning rate of $1e-5$ and a sequence length of 60, achieving a mean relative error of 2.11% on seen initial conditions and 2.85% on unseen ones. For more details on the PINTO and PI-DeepONets hyperparameters, see A.

3.2 Burgers Equation

As the second test case, we consider the one-dimensional nonlinear Burgers equation used in modeling turbulence, fluid flows, gas dynamics and traffic flow. The Burgers equation is

$$\frac{\partial u}{\partial t} + u \frac{\partial u}{\partial x} = \nu \frac{\partial^2 u}{\partial x^2}, \quad (10a)$$

$$u(0, x) = u_0(x), \quad (10b)$$

where u_0 is the initial conditions and ν is the viscosity coefficient. The initial conditions $u_0(x) \sim \mathcal{N}(0, \sigma^2)$ are sampled from a Gaussian random field with mean zero and covariance determined by the Laplacian Li et al. (2020a). We use periodic boundary conditions and set $\nu = 0.01$. Here, PINTO is trained to learn the mapping between multiple initial conditions and the solution of the PDE. PINTO is trained for 80 different initial conditions with physics loss (Eq. 3) considering 2000 collocation, 250 initial and boundary points in the domain $[0, 1] \times [0, 1]$ and tested on 20 unseen initial conditions. Inference is performed on seen and unseen initial conditions for trained time and untrained time $t > 1$. Numerical solutions for validation are obtained using an off the shelf solver Li et al. (2020a).

Figure 5 shows the solution of the Burgers equation for two sets of seen and unseen initial conditions computed by PINTO. The corresponding numerical solution and the relative error are visualized to evaluate the performance of PINTO. Table 1 shows that the relative error for PI-DeepONet is three times that of our PINTO model for both seen and unseen initial conditions. Figure 6 shows the solution from PINTO, numerical solver, and PI-DeepONet at three discrete times $t = 0.01, 0.5, 2$ to illustrate how the solution evolves in time. $t = 2$ is a time step outside the temporal domain used to train all neural models. As time increases, the deviations of the solution computed by PINTO and PI-DeepONet from the numerical solution increase, but our PINTO model has fewer deviations compared to PI-DeepONet and has a better generalization for unseen initial conditions. The location with maximum value is marked with the letter A in Figure 5 to track how the solution evolves over time. We see that PINTO is able to maintain the extreme value of the solution better than PI-DeepONet. In addition, PINTO is able to maintain periodic boundary conditions better than PI-DeepONet.

A series of experiments similar to the Advection case have been performed to determine the number of CAUs for Burgers equations. Table. 2 summarizes the experiments with different learning rates and the number of CAUs, and its last column consists of the mean relative errors in the prediction of trained models on the set of unseen initial conditions.

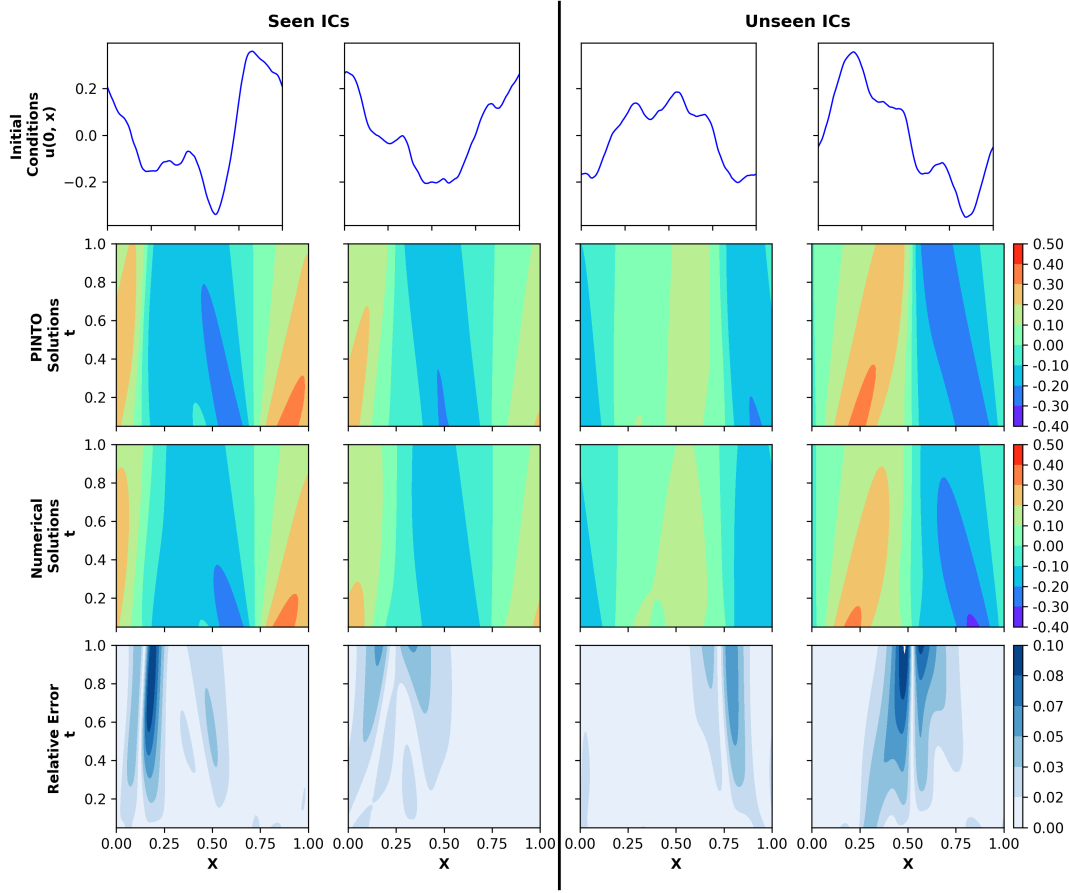


Fig. 5 Burgers Equation: Initial conditions (first row), PINTO solutions (second row), corresponding numerical solution (third row) and relative error of PINTO solution (fourth row) for seen (first two columns) and unseen (last two columns) initial conditions.

3.3 Navier-Stokes Equation

The next three test cases, viz., Kovasznay flow, Beltrami flow and lid driven cavity flow, are solutions of the Navier-Stokes equations

$$\frac{\partial \mathbf{u}}{\partial t} + (\mathbf{u} \cdot \nabla) \mathbf{u} = -\nabla p + \frac{1}{Re} (\nabla^2 \mathbf{u}), \quad (11a)$$

$$\nabla \cdot \mathbf{u} = 0, \text{ in } \Omega, \quad (11b)$$

$$\mathbf{u} = \mathbf{g}, \text{ on } \partial\Omega, \quad (11c)$$

where \mathbf{u} is the velocity vector, p is the pressure, Re is the Reynolds number and \mathbf{g} is the initial/boundary condition. For validation, we use the analytical solution of the Kovasznay and Beltrami flows, and the numerical solution from

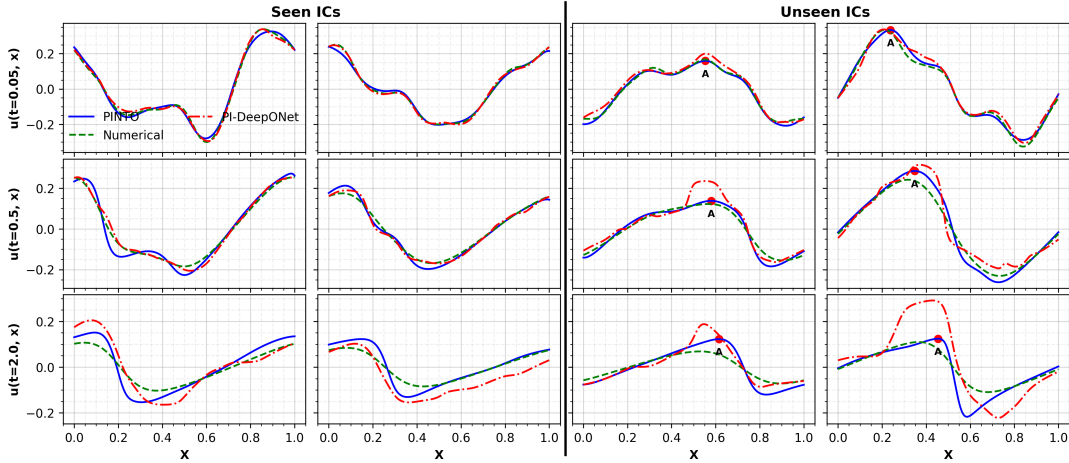


Fig. 6 Burgers Equation: PINTO, PI-DeepONet and numerical solutions for seen and unseen initial conditions at $t=0.01, 0.5, 2$. The first two columns are results for seen and the last two columns are for the unseen initial conditions. A landmark A is shown in the solution for unseen initial conditions (ICs) to visualize how the wave is propagating in time.

a finite volume solver for the lid driven cavity flow. In what follows, we discuss each test case in detail.

3.3.1 Kovaszny Flow

The Kovaszny flow is governed by the steady-state Navier-Stokes equation (first term of eq. 11a is 0) and has the following analytical solution

$$\begin{aligned} u(x, y) &= 1 - e^{\zeta x} \cos(2\pi y), \\ v(x, y) &= \frac{\zeta}{2\pi} e^{\zeta x} \sin(2\pi y), \\ p(x, y) &= \frac{1}{2}(1 - e^{2\zeta x}), \end{aligned}$$

where $\zeta = 0.5\text{Re} - \sqrt{0.25(\text{Re})^2 + 4\pi^2}$. We consider the domain $[-0.5, 1.0] \times [-0.5, 1.5]$. To numerically solve the Navier-Stokes equations for the Kovaszny flow, boundary conditions are provided to the solver by evaluating the analytical solution at the boundary. Changing the value of Re changes the boundary condition. In this test case, PINTO learns the mapping between the boundary conditions and the solution of the PDE.

For training PINTO, 2000 domain collocation points and 254 boundary points are used. A sequence length of 80 is used for the BPE and BVE units. The boundary values of the BVE input sequence are x -directional velocity, y -directional velocity, and pressure. As the output is the vector (u, v, p) , PINTO has three separate output units for u , v , and p , each with 2 hidden dense layers (64 neurons). Training is performed by minimizing the physics loss Eq. 3

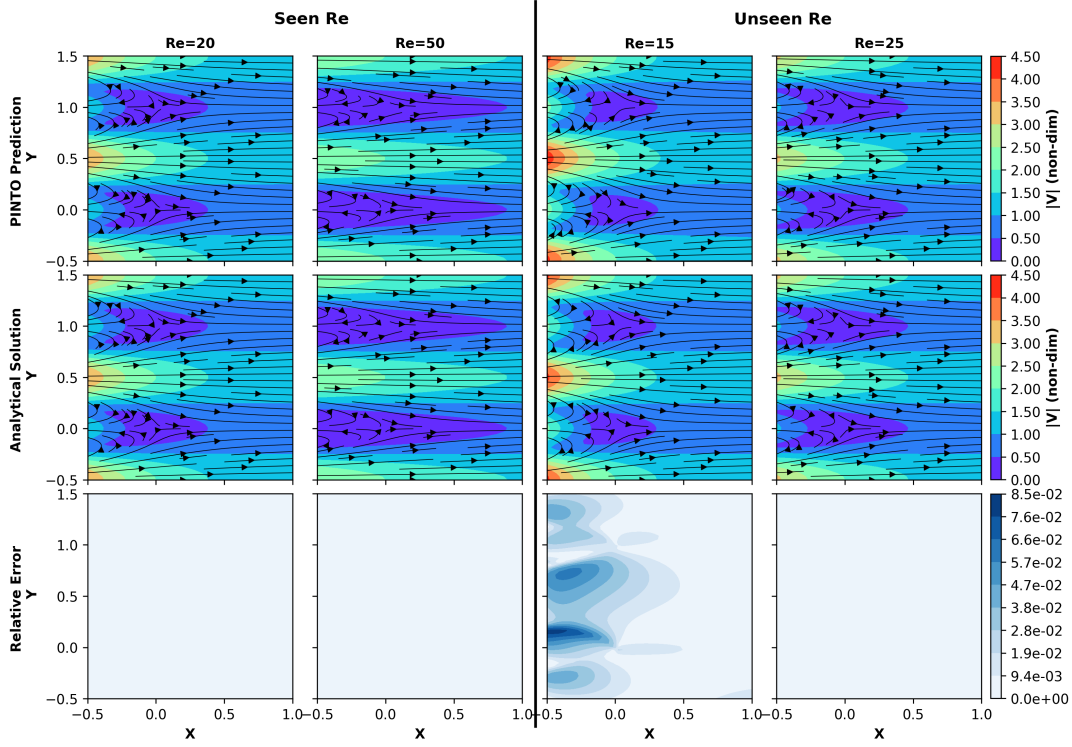


Fig. 7 Kovasznay Flow: PINTO solutions (first row), corresponding analytical solution (second row) and relative error of PINTO solution (fourth row) for seen (first two columns) and unseen (last two columns) initial conditions (Re). Flow streamlines are overlaid on a background of the velocity magnitude $|V| = \sqrt{u^2 + v^2}$ for the solution. Only magnitude of relative error is shown.

for 40,000 epochs using the Adam optimizer with a learning rate of $5e - 4$. The PI-DeepONet is also trained in the same setting for comparison. We used the relative error in the total velocity magnitude ($|V| = \sqrt{u^2 + v^2}$) as a performance metric to evaluate PINTO and PI-DeepONet.

To examine the generalization of the neural model to various boundary conditions in the Kovasznay flow, both the PINTO and PI-DeepONet models are first trained for boundary conditions corresponding to $Re = 20, 30, 50,$ and 80 . The trained model is then used to simulate the solution for unseen boundary conditions corresponding to 20 different Reynold's numbers, which are randomly generated between 10 and 100. Table 1 presents the mean relative error comparisons between the trained PINTO and PI-DeepONet model simulations for both seen and unseen boundary conditions. Overall, the relative error is low for both neural architectures for the seen boundary conditions. The relative error for PI-DeepONet is 2 times for seen and 5 times for unseen conditions, compared to our PINTO model, showing the latter's superior performance.

The 2D field of the solution is visualized using a 64×64 grid (Figure 7). The PINTO solution, the analytical solution, and the relative error are shown for two sets of seen ($Re = 20$ and 50) and unseen ($Re = 15$ and 25) boundary conditions. As the Kovaszny flow is a steady flow, time is not considered here. We see that the visual quality of the solution matches the low relative error for our PINTO model reported in Table 1. Overall, the findings demonstrate that our PINTO model can successfully generalize to unseen boundary conditions.

3.3.2 Beltrami Flow

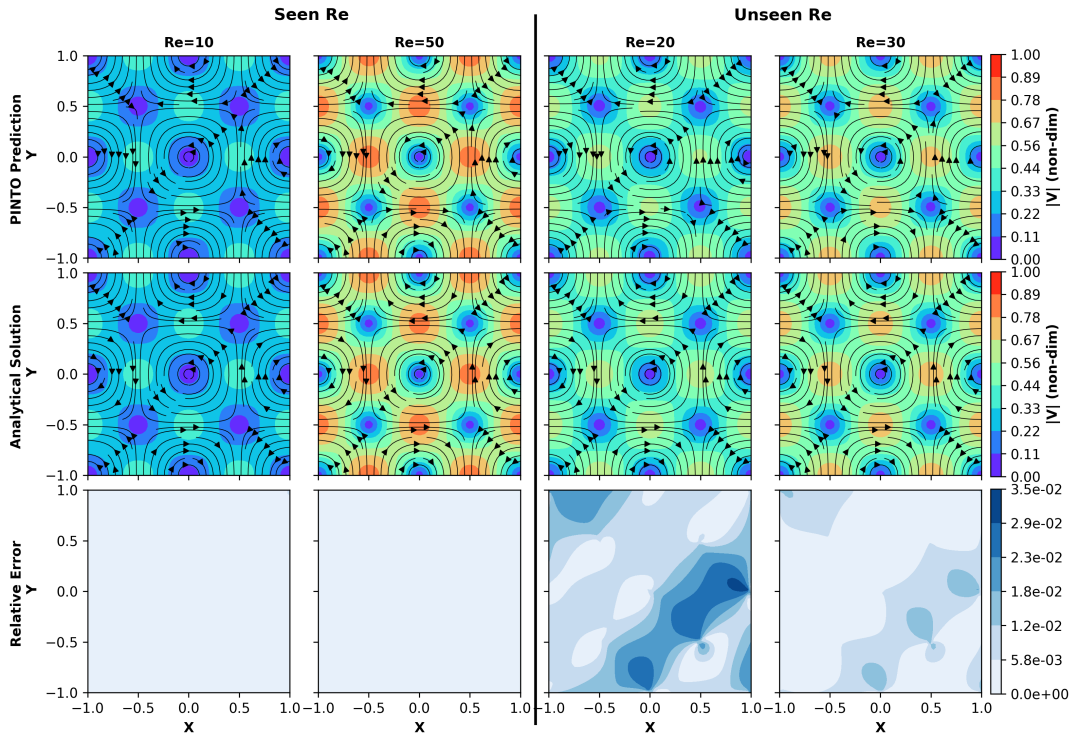


Fig. 8 Beltrami Flow: PINTO solutions (first row), corresponding analytical solution (second row) and relative error of PINTO solution (fourth row) for seen (first two columns) and unseen (last two columns) initial conditions (Re) at solution time step $t = 0.5$. Flow streamlines are overlaid on a background of the velocity magnitude $|V| = \sqrt{u^2 + v^2}$ for the solution. Only magnitude of relative error is shown.

The Beltrami flow is governed by the unsteady Navier-Stokes equation (Eq. 11), with a dynamic spatially varying boundary condition. This flow has

an analytical solution given by

$$\begin{aligned} u(x, y, t) &= -\cos \pi x \sin \pi y e^{-2\pi^2 \nu t}, \\ v(x, y, t) &= \sin \pi x \cos \pi y e^{-2\pi^2 \nu t}, \\ p(x, y, t) &= -\frac{\cos 2\pi x + \cos 2\pi y}{4} e^{-4\pi^2 \nu t}, \end{aligned}$$

where $\nu = 1/\text{Re}$. Similar to the previous test case, the numerical solvers are given the initial and boundary condition obtained from the analytical expression. Changing the Reynolds number gives multiple sets of initial and boundary conditions. In total, 5000 collocation points are sampled from the given spatiotemporal domain, 1000 boundary condition points (250 from each of the 4 sides), and 500 initial condition points. The same model configuration and hyperparameter choice as for the PINTO model for Kovaszny flow is used here.

The PINTO model was trained for boundary conditions corresponding to $\text{Re} = 10, 50, \text{ and } 100$. Subsequently, simulations are performed using the trained model for unseen boundary conditions corresponding to 20 different Re generated randomly between 10 and 150. In Figure 8, the first two columns show the comparison between the predictions from PINTO and the analytical solution for seen boundary conditions during training, and the last two columns show the comparison for unseen boundary conditions during testing. Table 1 summarizes the mean relative error in the time interval of $[0, 2]$ for the seen and unseen boundary conditions.

3.3.3 Lid Driven Cavity Flow

We simulate the steady-state Navier-Stokes equation for the lid-driven flow at a Reynolds number of 50 (Eq. 11 with first term zero, $\text{Re}=50$) in a computational domain $[0, 1] \times [0, 1]$. Since the only boundary that changes is the lid's velocity, here we learn the mapping between lid velocities (the top boundary condition) to the solution space. In the domain, we considered 2000 collocation points and 400 boundary points (100 on each side of the boundary). Here, the boundary condition is the velocity of the lid. During training, we used the lid velocities of 1, 2, and 3. Figure 9 shows the comparison plots between PINTO prediction and numerical solutions for seen lid velocities of 1 and 2 during training in the first two columns and for unseen lid velocities of 1.5 and 2.5 in the last two columns inside. Table 1 documents the mean relative error in the predictions of the PINTO on the 64×64 grid for the seen and unseen lid velocities. For validation, numerical solutions for all lid velocities during training and testing are simulated from the Finite Volume code (Ueckermann and Lermusiaux, 2012). Figure 10 compares PINTO and PI-DeepONet solutions for unseen lid velocities between 1 and 3 (the values seen during training) and greater than 3 (outside the range of values seen during training). For the lid velocity of 1.2, the PINTO and PI-DeepONet solutions are accurate and comparable to the numerical solution, whereas, for the lid velocity of 3.5, the PINTO solutions

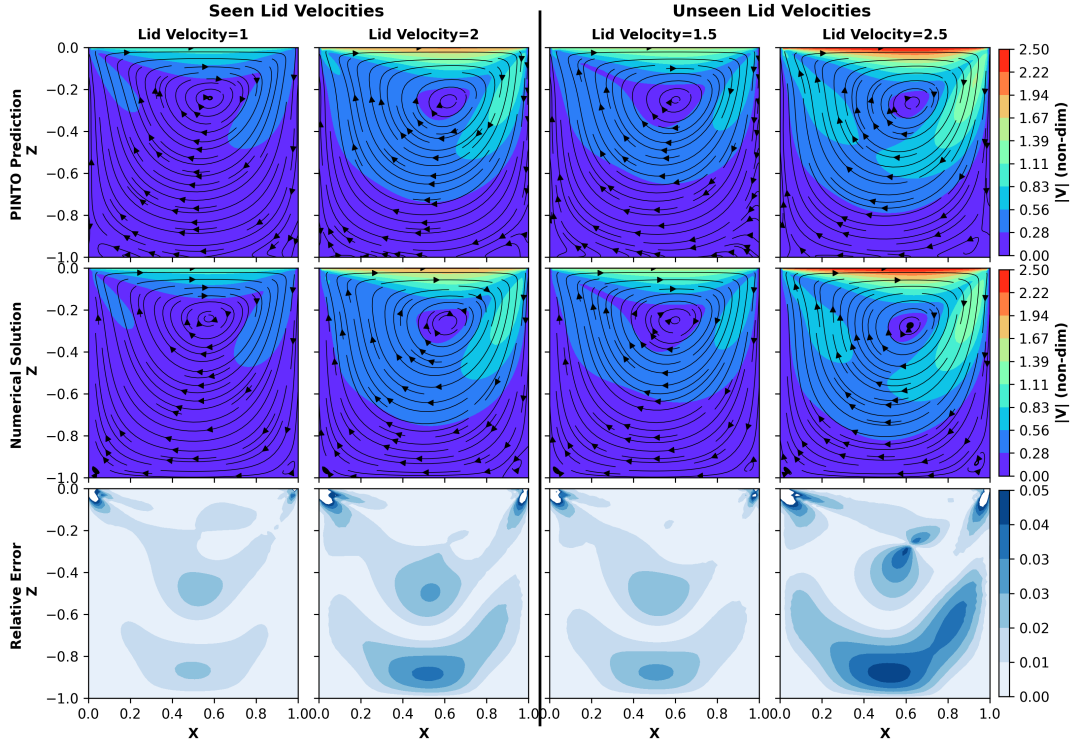


Fig. 9 Lid Driven Cavity Flow: PINTO solutions (first row), corresponding analytical solution (second row) and relative error of PINTO solution (fourth row) for seen (first two columns) and unseen (last two columns) boundary conditions (Lid Velocity). Flow streamlines are overlaid on a background of the velocity magnitude $|V| = \sqrt{u^2 + v^2}$ for the solution. Only magnitude of relative error is shown.

are better compared to the PI-DeepONet solutions. For PI-DeepONet, in this challenging test, the relative error crosses 12% at several grid points, making the solution unusable. In general, the relative error for different unseen lid velocities from the PINTO solution is 2.78%, which is less than half of the relative error (6.08%) of the PI-DeepONet solution.

4 Discussion

In this section, we discuss computational complexity, the need for a neural operator, the interpretation of our neural operator from the point of view of classical numerics, comparison to other neural operators, insights into how the cross-attention unit can enhance other neural operators, and limitations.

Computational complexity: Generally, transformer operators are computationally intensive due to the attention matrix. In addition, transformer-based neural operators Hao et al. (2023) require extensive simulation or ob-

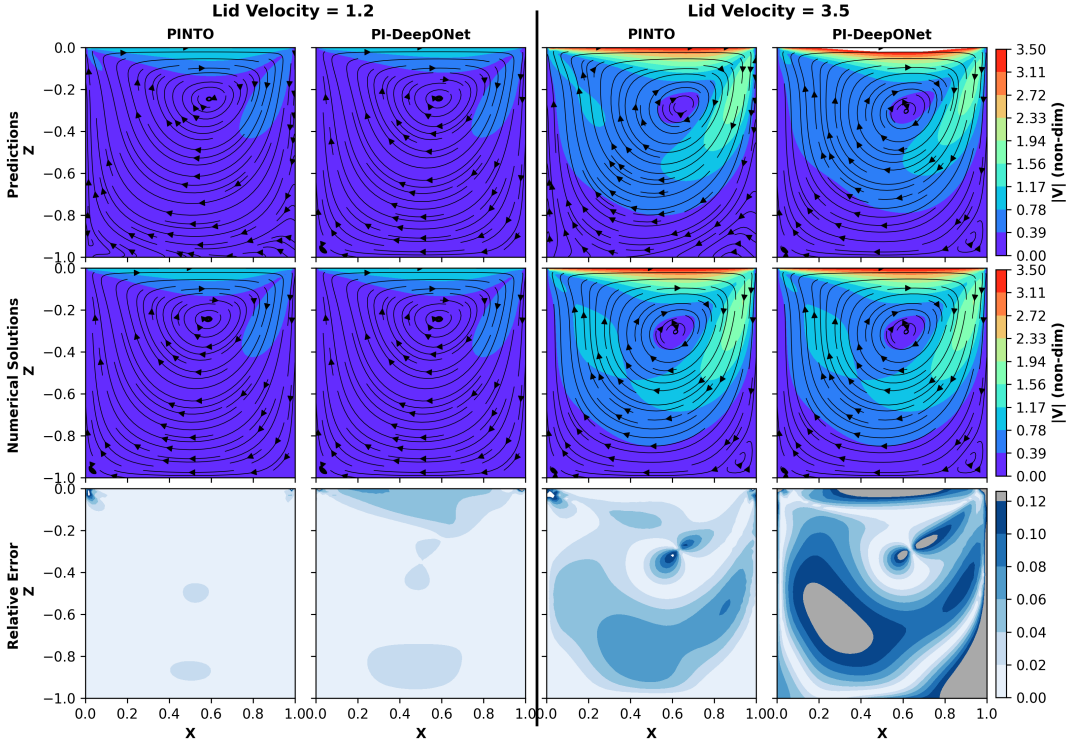


Fig. 10 Lid Driven Cavity Flow: PINTO and PI-DeepONet solutions (first row), corresponding numerical solution (second row) and relative error (third row) for unseen lid velocity interpolation (1.2) and extrapolation (3.5). Flow streamlines are overlaid on a background of the velocity magnitude $|V| = \sqrt{u^2 + v^2}$ for the solution. Only magnitude of relative error is shown.

servational data to learn to generalize to irregular meshes and multiple input functions. In contrast, PINTO achieves generalization using cross-attention units trained by minimizing the physics-loss. As the query point is a sequence of length $M = 1$, the complexity of PINTO’s attention mechanism is $O(N \times n_e^2)$, as opposed to $O(MN \times n_e^2)$ of general attention, where M, N represents query and key sequence lengths and n_e is the embedding dimension.

Need of a neural operator: Vanilla PINNs learn a mapping between the input domain and the solution space $\mathcal{G} : \Omega \mapsto \mathcal{H}$ that satisfies the differential operator for a specific initial/boundary condition. Here, $\mathcal{G}_\theta(\mathbf{x}; \Theta)$ is a deep neural network with Θ as parameters that approximate $h \in \mathcal{H}$ of Eq. 1. To obtain the optimal parameters of the network (Θ^*), we solve the following optimization problem.

$$\min_{\theta} \frac{1}{N_c} \sum_{j=1}^{N_c} |f_c^j - \mathcal{N}(\mathcal{G}(\theta; X_c^j); \alpha)|^2 + \frac{1}{N_{ib}} \sum_{j=1}^{N_{ib}} |b_{ib}^j - \mathcal{B}(\mathcal{G}(\theta; X_{ib}^j))|^2, \quad (12)$$

where, $\{(X_{ib}^j, b_{ib}^j)\}_{j=1}^{N_{ib}}$ denote the training data points on $\partial\Omega$, and $\{X_c^j\}_{j=1}^{N_c}$ are the training points (called collocation points) on the domain Ω . $\mathcal{G}(X; \Theta^*)$ is an approximate solution to Eq. 1 for a given b . For a different b , the optimization problem in Eq. 4 must be solved again to obtain another set of optimal parameters (Θ^*). In other words, PINNs need retraining if the initial and boundary conditions change. A neural operator framework is necessary to generalize to different initial and boundary conditions. However, the neural operators in the literature are trained using simulation data, hence we proposed our neural operator that efficiently generalizes to different initial/boundary conditions while training with physics-loss.

Interpretation from classical numerics: Neural operators are akin to traditional numerical techniques, such as finite elements, substituting the linear span of local basis functions with neural operator layers Li et al. (2020a). The initial and boundary conditions ensure the necessary constraints for a unique PDE solution, dictating the function space for the solution, so the network must learn to incorporate these conditions. Numerical methods involve discretizing the PDE Eq. 1 into a system of linear equations ($Ax = b$), providing solutions across the grid. Alternatively, the point solution corresponds to the weighted sum of the initial and boundary conditions ($x = A^{-1}b$). Interior points as queries, with initial and boundary points as keys and values in an attention mechanism, yield the weighted sum of boundary functions, mirroring numerical methods. The attention score combines two terms: (i) similarity and (ii) magnitude Song et al. (2021). The similarity term uses an RBF kernel with a length-scale hyperparameter to assess the query-key importance. Thus, our PINTO model can be viewed as a learning scheme inspired by traditional numerical methods, to us the attention mechanism for learning boundary-aware vectors.

Comparison to other neural operators: It is worth noting that traditional physics-informed neural networks or neural operators require separate training for each set of initial/boundary conditions, whereas our PINTO model allows training once for multiple initial/boundary conditions and can handle unseen conditions during inference. The physics-informed DeepONet (PI-DeepONet) (Lu et al., 2021a; Goswami et al., 2023) used in the present paper for the comparison of PINTO was repurposed to find PDE solutions with different initial/boundary conditions. Unlike PI-DeepONet, PINTO allows different vector lengths to be used as input of the BPE and BVE units during training and testing rather than a fixed length. By means of the cross-attention mechanism, the query point’s representation vector effectively captures all the relevant information from the boundary points and their values, which is necessary for predicting the PDE solution at that specific query point for any unseen boundary condition. As our goal was to train with physics-loss, other neural operator models such as physics-informed neural operators, Fourier neural operators, or convolutional neural operators that need simulation data for training at some resolution are not considered for comparison.

Unlike the DeepONet architecture (Lu et al., 2021a; Wang et al., 2021), one key novelty of PINTO is the treatment of the initial/boundary conditions

as a sequence of vectors, where each element is a vector of initial/boundary coordinates and values. In addition, PINTO uses an attention mechanism to learn the encoded representation of the initial/boundary functional space \mathcal{B} . This mode of representation not only helps in generalization but also gives the practical utility of using different lengths of boundary vectors during training and inference phases, making our approach further different from the branch and trunk nets (DeepONet).

Cross Attention Units in other neural operators: The kernel integral operator implemented using the cross-attention unit of PINTO is versatile. In PINTO, we used attention in the representation space of the domain’s coordinates and the initial/boundary conditions. In the Fourier Neural Operator, this mechanism can be incorporated by performing a cross attention between the input field and solution domain in the Fourier space. Time marching neural operators such as OFormer and GNOs can also benefit from the introduction of cross-attention units to condition the representation space with input functions.

Limitations: Since the training of the PINTO model uses collocation points and physics-loss, it may suffer spectral bias reported in other PINN models. There might also be training discrepancies due to imbalances in different terms in the loss functions. Adaptive training and dynamic weighting strategies (Jin et al., 2021; Daw et al., 2023; Hou et al., 2023; Maddu et al., 2022; Deguchi and Asai, 2023; Tang et al., 2023; Moseley et al., 2023) must be adopted to address these limitations.

5 Conclusion and Future Scope

Our newly developed PINTO architecture enhances the generalizability of neural models to solve IBVPs with multiple initial and boundary conditions. The key novelty of the architecture is the introduction of the new cross-attention unit that implements the attention-based integral kernel operator. This architecture is successful in transforming the representation vector of the PDE solution’s domain to a boundary/initial condition-aware encoding. Using five diverse test cases, we demonstrated that the relative error of the PINTO model is comparable for seen and unseen initial and boundary conditions. These results show that the encoding learned through our cross-attention unit is efficient in generalizing to new out-of-distribution (unseen during training) input functions of initial and boundary conditions. Comparative analysis with the PI-DeepONet neural operator model demonstrates the superior performance of PINTO to effectively generalize to unseen initial and boundary conditions. The relative error of PINTO solutions for all test cases in unseen testing configurations is low, only 20% to 33% of the relative error of PI-DeepONet’s solutions. We also show that PINTO is able to find solutions outside the temporal domain in which training is performed, the first result of this nature in the neural operator literature. Future directions of our work include the incorporation of turbulent dynamics into the PINTO framework. We envision that

Table 2 Mean relative error of PINTO predictions for different hyperparameters for Advection and Burgers equation. Here, the mean of relative error across all the test cases is indicated as the validation metrics

Expt.	Cross Attention Units	Epochs	Activation	Learning Rate	Sequence Length	Relative Error
Advection Equation						
1	1	40000	swish	$5e-5$	40	8%
2	1	40000	swish	$1e-5$	40	7.57%
3	1	40000	tanh	$1e-4$	40	7.98%
4	1	40000	tanh	$5e-5$	40	8.43%
5	1	40000	tanh	$1e-5$	40	7.21%
6	1	40000	tanh	$1e-5$	60	2.61%
7	1	40000	tanh	$1e-5$	80	2.534%
8	2	20000	swish	$1e-5$	40	4.88%
9	2	20000	tanh	$1e-5$	60	2.47%
Burgers Equation						
1	2	20000	tanh	$1e-3$	40	6.06%
2	3	20000	tanh	$1e-3$	40	5.58%
3	3	20000	tanh	Exponential Decay learning_rate= $1e-3$ decay_rate = 0.9 decay_steps = 10000	40	5.24%

the PINTO model will find applications in optimizing the layout of wind farms, building digital twins, modeling the earth system, and any other domain governed by initial boundary value problems. Moreover, the cross-attention units are versatile, hence, they could be used to devise architectures for geometry generalization as well. Incorporating uncertainty quantification schemes Guo et al. (2024); Zou et al. (2024) into PINTO and using it for inverse problems are also potential future directions Gao et al. (2024); Guo et al. (2022).

A Choice of hyperparameters:

Like any neural model, the performance of PINTO is influenced by the number of layers, units, the activation function, and other hyperparameters. Here, the decision of the number of cross-attention units (CAUs) in the second stage of PINTO, the sequence length of initial and boundary conditions, and the choice of training hyperparameters are made based on cross validation. Since here we are emphasizing the applicability of our proposed architecture to generalize for unseen initial and boundary conditions, we have chosen the hyperparameters that gave good predictions with low relative errors on the unseen conditions; alternatively, one can choose the optimal set of hyperparameters using the grid search algorithm or efficient search algorithms (Bergstra et al., 2011; Escapil-Inchauspé and Ruz, 2023; Kaplarević-Mališić et al., 2023; Wang and Zhong, 2024). Table 2 summarizes the hyperparameters selected for Advection and Burgers equations. For solving Navier Stokes equation, PINTO has learned the mapping with lesser relative errors (Table. 1) with a single CAU unit and shallow multi-layer perceptrons for lifting and projection units with activation function of Swish. Due to high imbalances in the boundary values for lid-driven cavity flow, while training both PINTO and PI-DeepONet, the loss term with 0 boundary value has given a weight of 100.

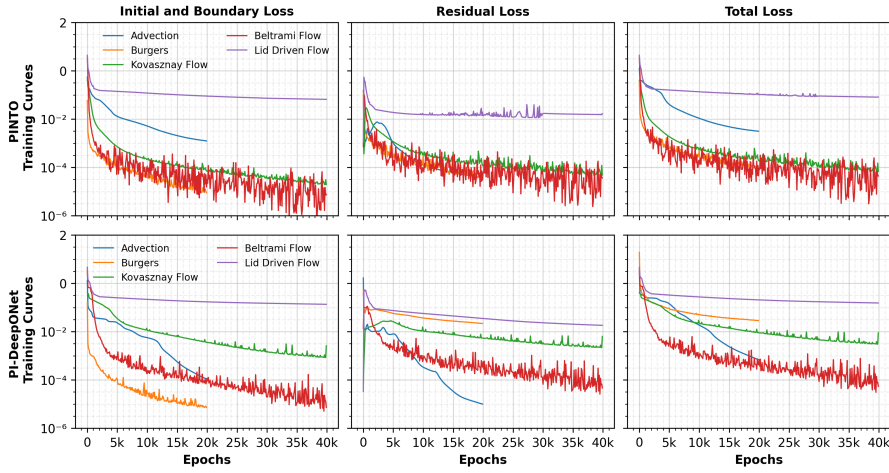


Fig. 11 Loss curves during training of PINTO (top row) and PI-DeepONet (bottom row) models for all test cases.

B Hyperparameters and Learning Curves

Learning curves during training of PINTO and PI-DeepONet for the five test cases are shown in Figure 11. For a fair comparison between the PINTO and PI-DeepONet solutions, the models are built approximately with the same number of trainable parameters and have used similar training strategies to ensure their convergence. Table 3 gives information on the architecture of PINTO models. The hyperparameters required to train the PINTO and PI-DeepONet models are tabulated in Table. 4.

Table 3 Hyperparameters in building PINTO model for each numerical example.

Test Case	# Parameters		QPE, BPE, BVE		Cross-Attention Unit			Output	
	PINTO	PI DeepONets	Layers	Units	MHA heads	key_dim	# CAUs	Layers (Units)	Layers (Units)
Advection Equation	100289	109400	2	64	2	64	2	2(64)	2(64)
Burgers Equation	141825	208896	2	64	2	64	3	2(64)	2(64)
Kovaszny Flow	75779	69568	2	64	2	64	1	1(64)	2(64)
Beltrami Flow	75779	69568	2	64	2	64	1	1(64)	2(64)
Lid Driven Cavity Flow	112834	91264	2	64	2	64	1	2(64)	2(64)

Table 4 Hyperparameters required to train the PINTO and PI-DeepONet model for all considered numerical examples.

Test Case	Epochs	Domain Points	Num. Batches	Optimizer		LR Scheduler	Sequence Length	
				Type	Learning Rate		PINTO	PI- Deep-ONets
Advection Equation	20000	2000	10	Adam	$1e-5$	-	60	80
Burgers Equation	20000	2000	6	Adam	$1e-3$	Exponential rate=0.9 steps=10000	40	80
Kovaszny Flow	40000	2000	5	Adam	$5e-4$	-	80	
Beltrami Flow	40000	5000	5	Adam	$1e-4$	-	100	
Lid Driven Cavity Flow	50000	5000	5	AdamW	$1e-3$	PiecewiseConstant boundaries [5000, 10000] values [$1e-3, 1e-4, 1e-5$]	40	

Data Availability

All data and code used and developed in the current work have been made publicly available through Github and Zenodo Kumar (2024).

Acknowledgements We thank the members of our QUEST Lab at the Indian Institute of Science Bangalore for useful discussions, especially Rishi Jinka and Azhar Gafoor. This work was partially funded by research grants from the Ministry of Earth Sciences (MoES/36/OOIS/Extra/84/2022) and Shell India Private Limited, Bangalore.

References

- Arcucci R, Moutiq L, Guo YK (2020) Neural assimilation. In: Computational Science–ICCS 2020: 20th International Conference, Amsterdam, The Netherlands, June 3–5, 2020, Proceedings, Part VI 20, Springer, pp 155–168
- Bergstra J, Bardenet R, Bengio Y, Kégl B (2011) Algorithms for hyper-parameter optimization. *Advances in neural information processing systems* 24
- Bonev B, Kurth T, Hundt C, Pathak J, Baust M, Kashinath K, Anandkumar A (2023) Spherical fourier neural operators: Learning stable dynamics on the sphere. In: International conference on machine learning, PMLR, pp 2806–2823
- Breton SP, Sumner J, Sørensen JN, Hansen KS, Sarmast S, Ivanell S (2017) A survey of modelling methods for high-fidelity wind farm simulations using large eddy simulation. *Philosophical Transactions of the Royal Society A: Mathematical, Physical and Engineering Sciences* 375(2091):20160097, DOI 10.1098/rsta.2016.0097, URL <https://royalsocietypublishing.org/doi/abs/10.1098/rsta.2016.0097>, <https://royalsocietypublishing.org/doi/pdf/10.1098/rsta.2016.0097>
- Cai S, Mao Z, Wang Z, Yin M, Karniadakis GE (2021) Physics-informed neural networks (pinns) for fluid mechanics: A review. *Acta Mechanica Sinica* 37(12):1727–1738

- Cao Q, Goswami S, Karniadakis GE (2024) Laplace neural operator for solving differential equations. *Nature Machine Intelligence* 6(6):631–640
- Cao S (2021) Choose a transformer: Fourier or galerkin. In: Ranzato M, Beygelzimer A, Dauphin Y, Liang P, Vaughan JW (eds) *Advances in Neural Information Processing Systems*, Curran Associates, Inc., vol 34, pp 24924–24940
- Chennault A, Popov AA, Subrahmanya AN, Cooper R, Rafid AHM, Karpatne A, Sandu A (2021) Adjoint-matching neural network surrogates for fast 4d-var data assimilation. arXiv preprint arXiv:211108626
- Chowdhury R, Murugan R, Subramani D (2023) Intelligent onboard routing in stochastic dynamic environments using transformers. In: *Proceedings of the 2023 International Conference on Autonomous Agents and Multiagent Systems*, pp 1688–1696
- Daw A, Bu J, Wang S, Perdikaris P, Karpatne A (2023) Mitigating propagation failures in PINNs using evolutionary sampling. URL <https://openreview.net/forum?id=Jz1iv-bxZ1a>
- Deguchi S, Asai M (2023) Dynamic & norm-based weights to normalize imbalance in back-propagated gradients of physics-informed neural networks. *Journal of Physics Communications* 7(7):075005
- Escapil-Inchauspé P, Ruz GA (2023) Hyper-parameter tuning of physics-informed neural networks: Application to helmholtz problems. *Neurocomputing* 561:126826
- Fablet R, Chapron B, Drumetz L, Mémin E, Pannekoucke O, Rousseau F (2021) Learning variational data assimilation models and solvers. *Journal of Advances in Modeling Earth Systems* 13(10):e2021MS002572
- Fanaskov VS, Oseledets IV (2023) Spectral neural operators. In: *Doklady Mathematics*, Springer, vol 108, pp S226–S232
- Gao Z, Yan L, Zhou T (2024) Adaptive operator learning for infinite-dimensional bayesian inverse problems. *SIAM/ASA Journal on Uncertainty Quantification* 12(4):1389–1423
- George RJ, Zhao J, Kossaifi J, Li Z, Anandkumar A (2024) Incremental spatial and spectral learning of neural operators for solving large-scale pdes. 2211.15188
- Goswami S, Yin M, Yu Y, Karniadakis GE (2022) A physics-informed variational deep-onet for predicting crack path in quasi-brittle materials. *Computer Methods in Applied Mechanics and Engineering* 391:114587
- Goswami S, Bora A, Yu Y, Karniadakis GE (2023) Physics-informed deep neural operator networks. In: *Machine Learning in Modeling and Simulation: Methods and Applications*, Springer, pp 219–254
- Goswami S, Jagtap AD, Babaee H, Susi BT, Karniadakis GE (2024) Learning stiff chemical kinetics using extended deep neural operators. *Computer Methods in Applied Mechanics and Engineering* 419:116674
- Guo L, Wu H, Yu X, Zhou T (2022) Monte carlo fpinns: Deep learning method for forward and inverse problems involving high dimensional fractional partial differential equations. *Computer Methods in Applied Mechanics and Engineering* 400:115523
- Guo L, Wu H, Wang Y, Zhou W, Zhou T (2024) Ib-uq: Information bottleneck based uncertainty quantification for neural function regression and neural operator learning. *Journal of Computational Physics* 510:113089
- Gupta G, Xiao X, Bogdan P (2021) Multiwavelet-based operator learning for differential equations. *Advances in neural information processing systems* 34:24048–24062
- Haghighat E, bin Waheed U, Karniadakis G (2024) En-deeponet: An enrichment approach for enhancing the expressivity of neural operators with applications to seismology. *Computer Methods in Applied Mechanics and Engineering* 420:116681
- Hao Z, Wang Z, Su H, Ying C, Dong Y, Liu S, Cheng Z, Song J, Zhu J (2023) Gnot: A general neural operator transformer for operator learning. In: *International Conference on Machine Learning*, PMLR, pp 12556–12569
- He J, Kushwaha S, Park J, Koric S, Abueidda D, Jasiuk I (2024) Sequential deep operator networks (s-deeponet) for predicting full-field solutions under time-dependent loads. *Engineering Applications of Artificial Intelligence* 127:107258
- Heermann DW, Burkitt AN (2012) *Parallel algorithms in computational science*, vol 24. Springer Science & Business Media
- Hou J, Li Y, Ying S (2023) Enhancing pinns for solving pdes via adaptive collocation point movement and adaptive loss weighting. *Nonlinear Dynamics* 111(16):15233–15261

- Ion IG, Loukrezis D, De Gersem H (2022) Tensor train based isogeometric analysis for pde approximation on parameter dependent geometries. *Computer Methods in Applied Mechanics and Engineering* 401:115593
- Jafarzadeh S, Silling S, Liu N, Zhang Z, Yu Y (2024) Peridynamic neural operators: A data-driven nonlocal constitutive model for complex material responses. *Computer Methods in Applied Mechanics and Engineering* 425:116914
- Jin P, Meng S, Lu L (2022) Mionet: Learning multiple-input operators via tensor product. *SIAM Journal on Scientific Computing* 44(6):A3490–A3514
- Jin X, Cai S, Li H, Karniadakis GE (2021) Nsfnets (navier-stokes flow nets): Physics-informed neural networks for the incompressible navier-stokes equations. *Journal of Computational Physics* 426:109951
- Kaplarević-Mališić A, Andrijević B, Bojović F, Nikolić S, Krstić L, Stojanović B, Ivanović M (2023) Identifying optimal architectures of physics-informed neural networks by evolutionary strategy. *Applied Soft Computing* 146:110646
- Karniadakis GE, Kevrekidis IG, Lu L, Perdikaris P, Wang S, Yang L (2021) Physics-informed machine learning. *Nature Reviews Physics* 3(6):422–440
- Kelley DH, Thomas JH (2023) Cerebrospinal fluid flow. *Annual Review of Fluid Mechanics* 55(1):237–264, DOI 10.1146/annurev-fluid-120720-011638, URL <https://doi.org/10.1146/annurev-fluid-120720-011638>, <https://doi.org/10.1146/annurev-fluid-120720-011638>
- Kovachki N, Lanthaler S, Mishra S (2021a) On universal approximation and error bounds for fourier neural operators. *Journal of Machine Learning Research* 22(290):1–76
- Kovachki N, Li Z, Liu B, Azizzadenesheli K, Bhattacharya K, Stuart A, Anandkumar A (2021b) Neural operator: Learning maps between function spaces. arXiv preprint arXiv:210808481
- Kovachki N, Li Z, Liu B, Azizzadenesheli K, Bhattacharya K, Stuart A, Anandkumar A (2023a) Neural operator: Learning maps between function spaces with applications to pdes. *Journal of Machine Learning Research* 24(89):1–97
- Kovachki N, Li Z, Liu B, Azizzadenesheli K, Bhattacharya K, Stuart A, Anandkumar A (2023b) Neural operator: Learning maps between function spaces with applications to pdes. *Journal of Machine Learning Research* 24(89):1–97, URL <http://jmlr.org/papers/v24/21-1524.html>
- Kovasznay LIG (1948) Laminar flow behind a two-dimensional grid. *Mathematical Proceedings of the Cambridge Philosophical Society* 44(1):58–62, DOI 10.1017/S0305004100023999
- Kumar BS (2024) quest-lab-iisc/pinto: Pinto. DOI 10.5281/zenodo.14330861, URL <https://doi.org/10.5281/zenodo.14330861>
- Lanthaler S, Mishra S, Karniadakis GE (2022) Error estimates for deeponeets: A deep learning framework in infinite dimensions. *Transactions of Mathematics and Its Applications* 6(1):tnac001
- Lehmann F, Gatti F, Bertin M, Clouteau D (2024) 3d elastic wave propagation with a factorized fourier neural operator (f-fno). *Computer Methods in Applied Mechanics and Engineering* 420:116718
- Li H, Ye X, Jiang P, Qin G, Wang T (2024a) Local neural operator for solving transient partial differential equations on varied domains. *Computer Methods in Applied Mechanics and Engineering* 427:117062
- Li W, Bazant MZ, Zhu J (2023a) Phase-field deeponet: Physics-informed deep operator neural network for fast simulations of pattern formation governed by gradient flows of free-energy functionals. *Computer Methods in Applied Mechanics and Engineering* 416:116299
- Li Z, Kovachki N, Azizzadenesheli K, Liu B, Bhattacharya K, Stuart A, Anandkumar A (2020a) Fourier neural operator for parametric partial differential equations. arXiv preprint arXiv:201008895
- Li Z, Kovachki N, Azizzadenesheli K, Liu B, Bhattacharya K, Stuart A, Anandkumar A (2020b) Neural operator: Graph kernel network for partial differential equations. arXiv preprint arXiv:200303485
- Li Z, Kovachki N, Azizzadenesheli K, Liu B, Stuart A, Bhattacharya K, Anandkumar A (2020c) Multipole graph neural operator for parametric partial differential equations. *Advances in Neural Information Processing Systems* 33:6755–6766

- Li Z, Meidani K, Farimani AB (2022) Transformer for partial differential equations' operator learning. arXiv preprint arXiv:220513671
- Li Z, Huang DZ, Liu B, Anandkumar A (2023b) Fourier neural operator with learned deformations for pdes on general geometries. *Journal of Machine Learning Research* 24(388):1–26
- Li Z, Kovachki N, Choy C, Li B, Kossaifi J, Otta S, Nabian MA, Stadler M, Hundt C, Azzizadenesheli K, et al. (2024b) Geometry-informed neural operator for large-scale 3d pdes. *Advances in Neural Information Processing Systems* 36
- Li Z, Zheng H, Kovachki N, Jin D, Chen H, Liu B, Azzizadenesheli K, Anandkumar A (2024c) Physics-informed neural operator for learning partial differential equations. *ACM/JMS Journal of Data Science* 1(3):1–27
- Lu L, Jin P, Pang G, Zhang Z, Karniadakis GE (2021a) Learning nonlinear operators via deepnet based on the universal approximation theorem of operators. *Nature machine intelligence* 3(3):218–229
- Lu L, Meng X, Mao Z, Karniadakis GE (2021b) Deepxde: A deep learning library for solving differential equations. *SIAM review* 63(1):208–228
- Maddu S, Sturm D, Müller CL, Sbalzarini IF (2022) Inverse dirichlet weighting enables reliable training of physics informed neural networks. *Machine Learning: Science and Technology* 3(1):015026
- Mandl L, Goswami S, Lambers L, Ricken T (2024) Separable deepnet: Breaking the curse of dimensionality in physics-informed machine learning. arXiv preprint arXiv:240715887
- Mittal R, Breuer K, Seo JH (2023) The flow physics of face masks. *Annual Review of Fluid Mechanics* 55(1):193–211, DOI 10.1146/annurev-fluid-120720-035029, URL <https://doi.org/10.1146/annurev-fluid-120720-035029>, <https://doi.org/10.1146/annurev-fluid-120720-035029>
- Moseley B, Markham A, Nissen-Meyer T (2023) Finite basis physics-informed neural networks (fbpinns): a scalable domain decomposition approach for solving differential equations. *Advances in Computational Mathematics* 49(4):62
- Navaneeth N, Chakraborty S (2023) Stochastic projection based approach for gradient free physics informed learning. *Computer Methods in Applied Mechanics and Engineering* 406:115842
- Navaneeth N, Tripura T, Chakraborty S (2024) Physics informed wno. *Computer Methods in Applied Mechanics and Engineering* 418:116546
- Pang G, D'Elia M, Parks M, Karniadakis GE (2020) npinns: nonlocal physics-informed neural networks for a parametrized nonlocal universal laplacian operator. algorithms and applications. *Journal of Computational Physics* 422:109760
- Pathak J, Subramanian S, Harrington P, Raja S, Chattopadhyay A, Mardani M, Kurth T, Hall D, Li Z, Azzizadenesheli K, et al. (2022) Fourcastnet: A global data-driven high-resolution weather model using adaptive fourier neural operators. arXiv preprint arXiv:220211214
- Peyvan A, Oommen V, Jagtap AD, Karniadakis GE (2024) Riemannonets: Interpretable neural operators for riemann problems. *Computer Methods in Applied Mechanics and Engineering* 426:116996
- Rafiq M, Rafiq G, Jung HY, Choi GS (2022) Ssno: Spatio-spectral neural operator for functional space learning of partial differential equations. *IEEE Access* 10:15084–15095
- Raissi M, Perdikaris P, Karniadakis G (2019) Physics-informed neural networks: A deep learning framework for solving forward and inverse problems involving nonlinear partial differential equations. *Journal of Computational Physics* 378:686–707, DOI <https://doi.org/10.1016/j.jcp.2018.10.045>, URL <https://www.sciencedirect.com/science/article/pii/S0021999118307125>
- Rani J, Tripura T, Kodamana H, Chakraborty S, Tamboli PK (2023) Fault detection and isolation using probabilistic wavelet neural operator auto-encoder with application to dynamic processes. *Process Safety and Environmental Protection* 173:215–228
- Raonic B, Molinaro R, De Ryck T, Rohner T, Bartolucci F, Alaifari R, Mishra S, de Bézenac E (2024) Convolutional neural operators for robust and accurate learning of pdes. *Advances in Neural Information Processing Systems* 36
- Richter L, Sallandt L, Nüsken N (2021) Solving high-dimensional parabolic pdes using the tensor train format. In: *International Conference on Machine Learning*, PMLR, pp 8998–

9009

- Shih B, Peyvan A, Zhang Z, Karniadakis GE (2025) Transformers as neural operators for solutions of differential equations with finite regularity. *Computer Methods in Applied Mechanics and Engineering* 434:117560
- Song K, Jung Y, Kim D, Moon IC (2021) Implicit kernel attention. In: *Proceedings of the AAAI Conference on Artificial Intelligence*, vol 35, pp 9713–9721
- Takamoto M, Praditia T, Leiteritz R, MacKinlay D, Alesiani F, Pflüger D, Niepert M (2022) Pdebench: An extensive benchmark for scientific machine learning. *Advances in Neural Information Processing Systems* 35:1596–1611
- Tang K, Wan X, Yang C (2023) Das-pinns: A deep adaptive sampling method for solving high-dimensional partial differential equations. *Journal of Computational Physics* 476:111868
- Taylor G (1923) Lxxv. on the decay of vortices in a viscous fluid. *The London, Edinburgh, and Dublin Philosophical Magazine and Journal of Science* 46(274):671–674
- Tiwari K, Krishnan N, et al. (2023) Cono: Complex neural operator for continuous dynamical systems. arXiv preprint arXiv:231002094
- Tripura T, Chakraborty S (2023) Wavelet neural operator for solving parametric partial differential equations in computational mechanics problems. *Computer Methods in Applied Mechanics and Engineering* 404:115783
- Ueckermann MP, Lermusiaux PFJ (2012) 2.29 Finite Volume MATLAB Framework Documentation. MSEAS Report 14, Department of Mechanical Engineering, Massachusetts Institute of Technology, Cambridge, MA, URL <http://mseas.mit.edu/?p=2567>
- Wang Q, Ihme M, Chen YF, Anderson J (2022a) A tensorflow simulation framework for scientific computing of fluid flows on tensor processing units. *Computer Physics Communications* 274:108292
- Wang S, Wang H, Perdikaris P (2021) Learning the solution operator of parametric partial differential equations with physics-informed deepONets. *Science advances* 7(40):eabi8605
- Wang S, Yu X, Perdikaris P (2022b) When and why pinns fail to train: A neural tangent kernel perspective. *Journal of Computational Physics* 449:110768
- Wang Y, Zhong L (2024) Nas-pinn: neural architecture search-guided physics-informed neural network for solving pdes. *Journal of Computational Physics* 496:112603
- Wen G, Li Z, Azizzadenesheli K, Anandkumar A, Benson SM (2022) U-fno—an enhanced fourier neural operator-based deep-learning model for multiphase flow. *Advances in Water Resources* 163:104180
- Wu P, Chang X, Yuan W, Sun J, Zhang W, Arcucci R, Guo Y (2021) Fast data assimilation (fda): Data assimilation by machine learning for faster optimize model state. *Journal of Computational Science* 51:101323
- Xu W, Lu Y, Wang L (2023) Transfer learning enhanced deepONet for long-time prediction of evolution equations. In: *Proceedings of the AAAI Conference on Artificial Intelligence*, vol 37, pp 10629–10636
- Yang L, Meng X, Karniadakis GE (2021) B-pinns: Bayesian physics-informed neural networks for forward and inverse pde problems with noisy data. *Journal of Computational Physics* 425:109913
- You H, Yu Y, D’Elia M, Gao T, Silling S (2022a) Nonlocal kernel network (nkn): A stable and resolution-independent deep neural network. *Journal of Computational Physics* 469:111536
- You H, Zhang Q, Ross CJ, Lee CH, Yu Y (2022b) Learning deep implicit fourier neural operators (ifnos) with applications to heterogeneous material modeling. *Computer Methods in Applied Mechanics and Engineering* 398:115296
- Zhao Z, Liu C, Li Y, Chen Z, Liu X (2024) Diffeomorphism neural operator for various domains and parameters of partial differential equations. arXiv preprint arXiv:240212475
- Zhu M, Feng S, Lin Y, Lu L (2023) Fourier-deeponet: Fourier-enhanced deep operator networks for full waveform inversion with improved accuracy, generalizability, and robustness. *Computer Methods in Applied Mechanics and Engineering* 416:116300
- Zou Z, Meng X, Psaros AF, Karniadakis GE (2024) Neuraluq: A comprehensive library for uncertainty quantification in neural differential equations and operators. *SIAM Review* 66(1):161–190